Influence of porosity on ice dynamic behavior as assessed by spalling tests

David Georges, Dominique Saletti, Maurine Montagnat, Pascal Forquin, Pascal Hagenmuller, David Hébert, Jean-Luc Rullier

Influence of porosity on ice dynamic behavior as assessed by spalling tests

D. Georges[a,b], D. Saletti[a], M. Montagnat[b], P. Forquin[a], P. Hagenmuller[c], D. Hébert[d], J-L. Rullier[d],

a. Univ. Grenoble Alpes, CNRS, Grenoble INP 1 , 3SR, F-38000 Grenoble, France

b. Univ. Grenoble Alpes, CNRS, Grenoble INP 1 , IGE, F-38000 Grenoble, France

c. Univ. Grenoble Alpes, CNRS, Grenoble INP 1 , CEN, F-38000 Grenoble, France

d. CEA CESTA (à compléter)

Abstract

The impact of hailstones remains a major issue due to the damage caused by hailstorms against aeronautical or space structures. During a such impact, an intense fragmentation develops in the hailstone due to dynamic tensile loading at high strain-rates which influences the mechanical loading transmitted to the impacted structure. Up to now, the work of Saletti et al. (2019) is the only survey providing a robust and reproductible set of experiments about the dynamic tensile strength of ice, however the microstructure influence was out the scope of this experimental study. Though, the hailstone microstructures are generally charaterised by a high level of porosity. It is the reason why the influence of this microstructural parameter on the dynamic behavior of polycrystalline ice needs to be investigated. The aim of this paper is to study the role of porosity on the tensile behavior of polycrystalline ice by applying the same experimental set-up and measurements processing than in Saletti et al. (2019) to low-porosity (LP) and high-porosity (HP) microstructures. To do so, spalling tests with a Hopkinson bar apparatus were conducted and fragmentation processes were carefully analyzed by means of an Ultra High Speed Camera, an Automatic Ice Texture Analyser and a micro-Computed Tomograph. The experimental results show that the tensile strength is sensitive to the applied strain rate for both types of micro-structures over the range 24 s^{-1} to 120 s^{-1}. A weakening effect of porosity is also observed, the lowly porous specimens being significantly stronger than the highly porous ones. The large

spherical pores present in the LP specimens are seen to contribute to this strength decrease. Although fragmentation analysis did not allow to clearly assess the role of these porosities on the crack initiation and propagation processes, the numerous clues such as the high number of cracks detected, the tortuosity of crack paths and the presence of porosities on the crack surfaces seem to validate the hypothesis of porosities playing a key role during ice fragmentation.

1 Introduction

Dynamic interactions between ice and man made structures are of concern in many situations, such as icebreaker ships crushing ice floe in polar regions, serac falls, atmospheric ice impacting buildings, aircrafts or even space shuttles. For the latter, NASA classified atmospheric ice as a potential source of damage after the catastrophic Columbia space shuttle break down in 2003. An accurate understanding of the ice dynamic strength failure is of interest to determine and to model the force generated during an impact and thus to provide relevant scaling of the structures of concern.

Dynamic confined compressive and tensile loadings are expected to developp in brittle materials under impact (Forquin et al., 2015; Forquin, 2017). Ice is known to behave as a brittle material at high strain-rates (Schulson and Duval, 2009), its mechanical response to dynamic confined compression and tension is thus essential and needs to be considered to get an accurate modelling. Up to now, with the improvement of computing capacities, numerous models have been developed to describe the behavior of polycrystalline ice during an impact event. Most of them adopted an elasto-plastic or elasto-visco-plastic approach, coupled with failure criterions (Carney et al., 2006; Pernas-Sánchez et al., 2012; Tippmann et al., 2013; Dousset, 2019). The ice behavior is assumed to be pressure dependent and the volumetric and deviatoric response of ice is different according to the direction of loading, compression or tension. The first models were manually adjusted by changing the material input parameters, the hardening modulus, the plastic failure strain and the compressive and tensile failure pressures, until a good correlation is reached between numerical simulations and experimental data (Kim and Kedward, 2000; Keune, 2004; Park and Kim, 2010). Thanks to the Split Hopkinson Pressure Bar technique (SHPB), the compressive yield stress sensitivity to strain-rate of ice was investigated (Kim and Keune,

2007; Shazly et al., 2009; Wu and Prakash, 2015). These experimental results, although scattered, reveal a strain-rate hardening behavior that has been implemented in recent modelling works (Pernas-Sánchez et al., 2012; Tippmann et al., 2013). These models are based on the strong hypothesis of a transition from a solid-to-liquid behavior of ice when reaching a tensile failure criterion. Above this threshold, ice is supposed to behave as a fluid, and not carry any shear or tensile stress. In most of the concerned models, the tensile failure stress is considered to be strain-rate insensitive and is either took from quasi-static experiment results or determined by a numerical parametric study. Indeed, for strain-rates lower than $10^{-1}\ s^{-1}$, the ice tensile strength remains constant and ranges between 0.5 MPa to 3 MPa, depending on the microstructural properties (Petrovic, 2003). However, other brittle materials, such as concrete and ceramics, are characterized by a dynamic tensile strength strongly dependent on the loading rate (Schuler et al., 2006; Erzar and Forquin, 2011, 2014; Zinszner et al., 2015). In order to take that into consideration, Ortiz et al. (2015) adapted the initial Mazars model (Mazars, 1984) to dynamic loadings and considered an ice tensile strength evolving similarly to the compressive strength with strain rate, but with values of strength one-tenth lower. While being the first attempt to catch the dynamic tensile behavior of ice, this approach was not based on any measurements performed under dynamic tensile conditions. This lack of knowledge is problematic as the tensile strength of ice material is the main driver of the fragmentation processes during impact events. This material property should be at the forefront among all the input parameters that should be identified in order to get satisfying modelling.

To our knowledge, only two studies experimentally investigated the response of ice dynamically loaded under tension. Lange and Ahrens (1983) tested ice specimens via plate impact experiments and measured a tensile strength of 17 MPa at a strain rate of $10^4\ s^{-1}$. Saletti et al. (2019) studied the strain rate sensitivity of ice dynamic tensile strength by performing spalling tests with a Hopkinson bar apparatus on isotropic polycrystalline ice. They observed a clear strain-rate hardening, the ultimate spalling strength was found to change from 2.3 MPa to 16.3 MPa for strain rates between 30 s^{-1} and 141 s^{-1}. Both studies have given little weight to the impact of defaults and specificities of the microstructures of the studied specimens. Under quasi-static tensile loading, grain size, crystallographic orientations and porosity, are expected

to impact the mechanical response of polycrystalline ice (Schulson and Duval, 2009). In particular, Kermani et al. (2008) and Timco et al. (1994) showed that the presence of porosity in atmospheric and sea ice respectively, significantly decreases their quasi-static tensile strength. Hailstone microstructures appear to be complex, and to strongly depend on the formation history, but clearly always present some porosity with a dispersed pore size distribution (see Macklin et al. (1977) for instance). More broadly, in many quasi-brittle materials, cracks are supposed to be triggered on the microstructural defects under tensile loading, such as porosities, grain boundaries, inclusions, sintering defects, etc.. At high strain-rates in tension an intense multiple fragmentation occurs as a result of the activation of numerous microstructural defects (Hild et al., 2003). In polycrystalline ice, and more specifically in hailstones, these microstructural defects can either be porosities, grain boundaries, impurities, micro-cracks, for instance. As mentioned before, owing to the presence of a high and complex porosity in hailstones, porosities might be the dominating defect population influencing the behavior of ice under dynamic loading. Quantifying how the defect of the microstructure can act upon ice fragmentation processes is therefore a key step to reach a better understanding of the behavior of ice under dynamic loading.

The present study will aim to evaluate how the porosity affects the dynamic tensile response of polycrystalline ice. To do so, two type of polycrystalline ice specimens, presenting different levels of porosity but similar grain size and shape, have been manufactured. The dynamic behavior of both types of specimen has been evaluated using the spalling technique on Hopkinson bar, according to the experimental procedure described in Saletti et al. (2019). The specimen growth method, the procedure for microstructure characterization and the spalling set-up are presented in section 2. In section 3.3, the dynamic tensile strength sensitivity to the strain-rate and porosity is analyzed. The influence of the porosity on the induced failure mechanisms is addressed in the discussion part via the analysis of crack initiation and propagation processes.

2 Materials and methods

2.1 Specimen growth and machining

The two studied materials are made of artificial polycrystalline granular ice grown in laboratory and are characterized by a microstructure with a low porosity (LP)($\approx 1-2\%$) and a microstruc-

ture with an high porosity (HP)($\approx 7-10\%$) respectively. Both microstructures are obtained using two growth techniques inspired by the one described in Barnes et al. (1971). Specimens are grown out of isotropic seeds made of crushed ice (with a maximum particle diameter of 2 mm) surrounded by water at 0°C. The slurry is placed on a Peltier element (-15°C), in a 0°C room, to grow gently from bottom to top, and avoid internal stresses during freezing. To obtain the LP microstructure, the isotropic seed is pumped before adding the water. The air trapped between the snow grains is maintained in order to produce the HP microstucture. The LP specimens have no visible porosities and are slightly opaque, whereas large porosities are visible in HP specimens. After unmolding, the specimens are stored during 24 hours in a 0°C environment. This annealing stage aims to relaxe freezing stress and to homogeneize the grain size. Finally, after lathing and milling, 120 mm long and 45 mm diameter cylindrical specimens are obtained. The geometric and density features of the specimens used in the spalling tests are listed in Table 1.

2.2 2D analysis of the microstructure : the Automatic Ice Texture Analyser (AITA)

Several LP and HP specimens, not tested here but assumed to be representative of the whole sets, were machined in thin square sections of approximately 50×50 cm^2 and 0.3 μm in thickness. Owing to the birefringent property of ice, the optical method of AITA (Wilson et al., 2003) gives access to the orientation of the **c**-axis (the optical axis) of the hexagonal crystal cell. The current assumption of a relative isotropic behavior in the plane normal to the **c**-axis (the basal plane) renders sufficient the knowledge of **c**-axis orientations. The AITA provides the **c**-axis orientations at a pixel scale set here to 20 μm, and therefore offers orientation images that enable to extract the 2D microstructure fabric and the crystallographic texture (plotted with orientation color-scaled images, see Figure 5).

2.3 3D analysis of the microstructure : micro Computed X-ray Tomography (microCT)

MicroCT is a convenient non destructive method to collect the 3D microstructure of a biphasic material when phases are X-Ray contrasted, and hence the porosities size and shape. Quantify-

Spec Id	Length (mm)	Diameter (mm)	Density (kg/m^3)
HP01	119.7	44.9	857
HP02	120.2	44.9	840
HP03	120.3	44.9	847
HP04	119.6	44.9	818
HP05	119.5	45.1	834
HP06	119.7	45.1	844
HP07	118.0	45.0	844
HP08	119.8	45.2	834
HP09	119.7	45.0	848
HP10	120.0	44.9	843
HP11	119.9	45.0	835
HP12	119.0	45.0	833
HP13	120.9	45.0	840
HP14	120.6	45.6	805
LP01	119.7	45.1	906
LP02	119.9	45.1	917
LP03	120.1	45.1	921
LP04	119.9	45.0	908
LP05	119.6	45.1	912
LP06	119.2	45.0	906
LP07	120.0	45.3	910
LP08	120.6	45.2	918
LP09	120.0	45.0	910
LP10	119.0	44.9	908
LP11	119.5	45.0	914
LP12	110.7	44.8	908

Table 1: Dimensions and densities of the specimens presented in this study. The calculation of the density using the mass and volume of the specimen delivers a typical uncertainty of individual values about $\pm$ 5 $kg.m^{-3}$.

ing damage in post-mortem specimens can also be achieved with microCT. Numerous scans with different resolutions were performed on HP and LP specimens in order to assess the homogeneity and the reproductibility of the pore structure. Here we present the scan configuration used with three HP specimens and three LP specimens scanned prior and after spalling tests. Detailed observations are given in the section 3.2 and 3.6.

2.3.1 Description of the microCT configuration (TomoCold)

Scans were performed in a cold room set at -20°C with the tomograph TomoCold DeskTom130 RX Solutions, specifically adapted to cold temperatures at the CNRM-CEN (Centres d'Etudes de la Neige), Grenoble. A voxel size of 27 μm was chosen, resulting from a compromise between the volume to be analyzed and the minimal resolution required to detect porosities in LP specimens. The X-ray tube was powered by a current of 238 μA and a voltage of 60 kV. The detector was composed of 1920 pixels $\times$ 1536 pixels with a physical pixel size of 127 μm. Each scan consisted of four stacks composed of 1440 radiographs covering a 360° rotation for every stack. One radiograph was computed as the average of two frames captured at three frames per second. The whole process for every scan lasted 1 h 15 min and the scanned specimens were subjected to spalling tests ($\varnothing \times h = 45 \times 120\ mm$).

2.3.2 Image post-processing

A 3D image is reconstructed from the acquired radiographs. A ring filter with a 20 voxel kernel was applied in order to remove ring features that are artefacts from the acquisition. After reconstruction the scans are composed of approximately $4500 \times 1660 \times 1660$ voxels, whose value spreads out between 0 (black) and 65536 (white). An enhancement of the contrast prior to conversion into 8 bit images was made in order to have reproducible grey level histograms. This operation allowed to apply identical thresholding method for each scan of the same microstructure (more below). Typical images (8 bits) of both microstructures are shown on Figures 1a and 2a. Examples of corresponding grey level probability density function are highlighted for each microstructure.

The threshold step allows to separate the voxels into two phases, i.e. air and ice, accord-

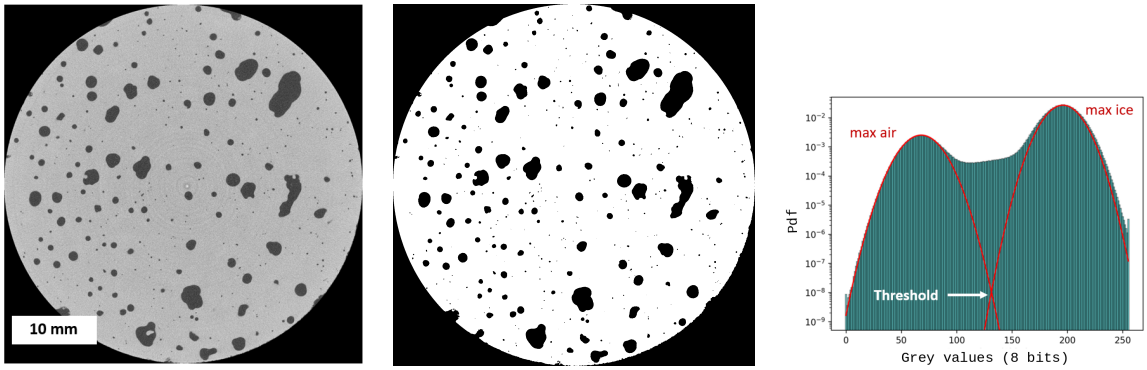

(a) (b) (c)

Figure 1: Slice of HP microstructure perpendicular to the specimen axis: (a) 8 bits image (b) Binary image (c) Probability Density Function of voxel grey levels

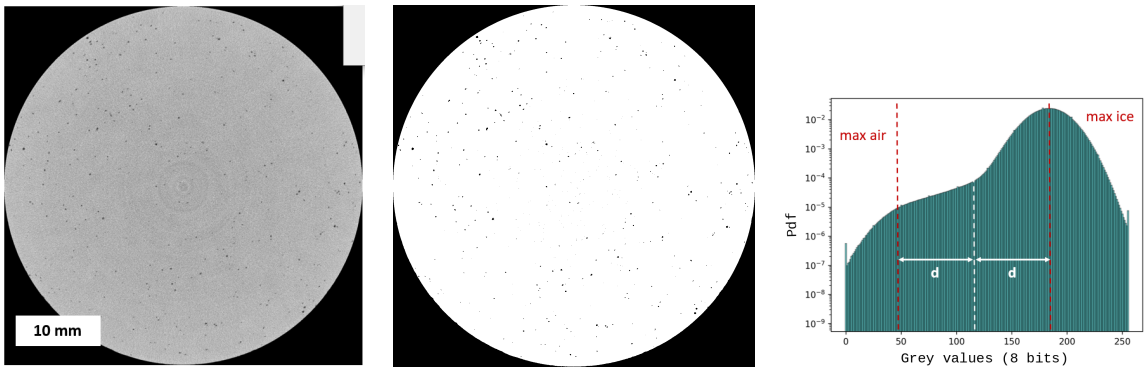

(a) (b) (c)

Figure 2: Slice of LP microstructure perpendicular to the specimen axis: (a) 16 bits image (b) Binary image *Need to add scale !!!*

ing to their grey level value. This operation has to be conducted with caution to minimize the error related to the image noise. HP microstructure histograms present two distinct maxima associated with each phase. Assuming that images are undergoing a Gaussian noise (related to the microCT device), the threshold value minimizing the voxel error is the intersection between the two Gaussian functions fitting each phase (red curves on Figure 1c). Finding a relevant threshold is more tricky for histograms associated to LP specimens, as the porosity density and size are much smaller. To do so, a pseudo-maximum for the air phase is manually picked, the threshold value is chosen to be the middle value between this maximum and the ice phase maximum. See Figures 1b and 2b to have an overview of the resulting binary images.

The segmentation stage has been performed on the binary images using SPAM (The Software for the Pratical Analysis of Materials), a Python package currently in development in the 3SR laboratory (Ref SPAM Eddy). During this stage each group of isolated or aggregated black voxels is labelled with a corresponding integer. Due to the presence of impulse noise (sparsely occurring white and black voxels) only labels whose volume exceeds 10 voxels, namely 0.19 mm^3 here, were taken into account and considered as porosities. The results of the analysis are presented in the Section 3.2.

2.4 The spalling technique

2.4.1 Experimental set-up

The spalling test on Hopkinson bar is a convenient technique to measure the tensile strength of quasi-brittle materials at strain-rate up to 200 s^{-1} (Klepaczko and Brara, 2001; Erzar and Forquin, 2010; Saletti et al., 2019) and to characterize the stress-strain relationship and tensile fracture energy of geomaterials (Pierron and Forquin, 2012; Lukić et al., 2018; Forquin et al., 2019b). A short compressive pulse generated by the impact of a cylindrical projectile against an incident bar propagates along the bar. When it reaches the interface bar/specimen a part of it is reflected because of an impedance discontinuity whereas the other part is transmitted to the specimen. The transmitted pulse is then reflected on the free surface as a tensile pulse creating a dynamic tensile loading inside the specimen when the amplitude of the latter is higher than the compressive pulse one. The core of the specimen undergoes an elastic deformation up to brittle

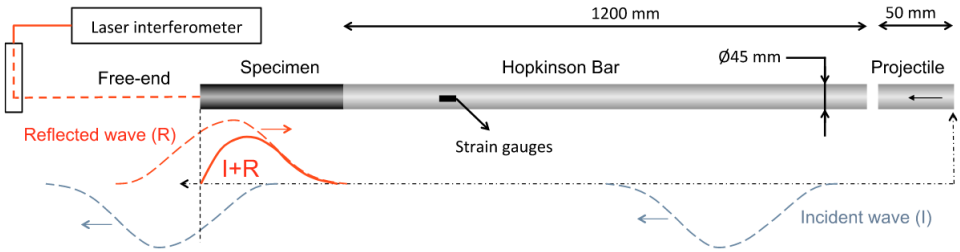

Figure 3: Scheme of the spalling test set-up used in the experiments, from Saletti et al. (2019)

fragmentation due to an intense dynamic tensile stress. Obviously this method is suitable for materials which compressive strength is higher than the tensile strength as it is the case for ice in the quasi-static regime (Schulson and Duval, 2009).

The configuration used here (Figure 3) is the same than the one described in Saletti et al. (2019) where further informations can be found. The projectile is 50 mm long and 45 mm in diameter and has a spherical-cap-ended nose acting as a pulse shaper, in order to smooth the loading pulse (Erzar and Forquin, 2010). The incident bar is 1200 mm long with the same diameter as the projectile. Both the projectile and the bar are made of high-strength aluminium alloy (yield strength $>$ 450 MPa) with a longitudinal wave speed C of 5078 $m.s^{-1}$, a density of 2800 $kg.m^{-3}$ and an elastic modulus equal to 72.2 GPa. The Hopkinson bar is instrumented with a strain gauge to measure the compressive pulse applied to the specimen. A reflective paper is glued at the free-end of the specimen allowing the measurement of the particle velocity of this rear face by a laser interferometer. The tests are filmed with an ultra high speed (UHS) camera (Kirana model from Specialised Imaging). For each test, 180 images with an inter-frame of 1 μs are obtained, the sensor resolution used is 924 pixels $\times$ 768 pixels.

As the major difficulty being the ambient temperature of the spalling room that far exceeds the ice melting temperature, several arrangements were made. The specimens are stored in a freezer set at -30°C located nearby their final position in the experimental set-up. A protocol was established in order to ensure that less than 45 seconds elapse between the time when the specimen is taken out from the freezer and the time when it is loaded in the spalling test apparatus. The full time of handling was systematically recorded for every test and remained below 45 seconds. A cylinder made of the same aluminium alloy as the one of the input bar is glued

on the specimen during its preparation in the cold room. This cylinder is 45 mm in diameter and two lengths were used, 30 mm and 40 mm. Its main roles are (i) to avoid a thermal shock between the ice specimen and the Hopkinson bar which is at room temperature; (ii) to delay the melting of the specimen on its face in contact with the bar. The post-mortem specimens were immediately taken back in the freezer after experiment when possible, namely if the fragmentation was not too intense.

2.4.2 Signal processing

Spalling strength to failure

As described in details in Erzar and Forquin (2010) and Saletti et al. (2019), from the signal measured one can use the linear acoustic approximation (Novikov et al., 1966) to deduce the ultimate spall strength σ_T of the specimen prior to fracture :

$$\sigma_T = \frac{1}{2}\rho_{ice} C_{ice} \Delta V_{pb}, \tag{1}$$

where ρ_{ice} is the specimen density and C_{ice} the longitudinal wave velocity in the specimen. The latter is computed by performing an inter-correlation between the rising stage of the strain gauge and laser signals to determine the time of propagation between the gauge location and the specimen free surface, the distance being perfectly known. ΔV_{pb} represents the pullback velocity corresponding to the difference between the maximum velocity and the velocity at rebound that are measured on the rear face of the specimen.

The Novikov approximation is relevant under certain assumptions. The deformation prior to fracture is assumed to be purely elastic in the core of the specimen likewise in the fragment bounded between the first fracture plane and the free surface. The specimen is assumed to undergo 1D longitudinal stress only, dispersion effects are neglected. In addition, a linear response is supposed prior the tensile stress peak, and the compressive and tensile Young's moduli are supposed to be equal (Forquin and Lukic 2018).

Evaluation of the strain rate during tensile loading

Gluing strain-gauges on an ice surface is challenging, especially in these experimental conditions where each second matters. The strain rate is estimated by means of elastic numerical simulations that are performed with the software ABAQUS-explicit. The material velocity profile of the free surface of each test (red curve in Figure 4a) is converted into an elastic profile (black curve in Figure 4a). This is achieved by keeping the slope of the tensile phase (that follow the maximum value of particle velocity profile) before the expected occurrence of spalling fracture characterized by the velocity rebound. By using the equation 1, a corresponding stress can be computed from the material velocity at a given time t. This stress profile is used as a loading pulse in the numerical simulations. The exact density and dimensions of each specimen was used for each computation. Figure 4b shows the type of curve obtained from the simulation to evaluate the strain rate in the tensile phase prior failure. For each test, the values are extracted from the results of the numerical simulation at the approximate location of the first appearance of cracks, thanks to the image sequence filmed during the test. The curve is valid up to the spall strength identified with equation 1. To get the minimum, maximum and mean value of the strain rate, the authors considered the stress interval which begins with the tensile phase ($\sigma > 0$) and ends with the ultimate spall strength measured (see gray zone in Figure 4b).

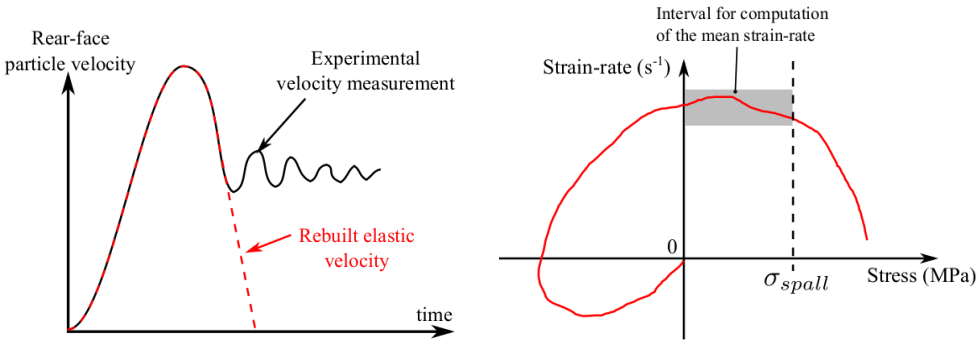

(a) (b)

Figure 4: (a) Rebuilt of the rear-face velocity to reproduce an virtual elastic loading in numerical simulations. (b) Interval of data taken into account to compute the mean strain-rate of a test (from Saletti et al. (2019))

2.4.3 Experimental indicators of test validity

Different indicators were considered to assess the quality of each test. As the major risk is the initiation of cracks due to compressive loading, the images of the UHS camera were carefully analyzed in order to detect any compressive damage. The post-mortem specimen part near the ice-bar interface is also checked with naked eyes, when specimens were fragmented in few pieces. Another source of error is the quality of the interfaces between (i) the aluminium insert and the specimen and (ii) the incident bar and the aluminium insert. For (i), the presence of water due to premature melting of the ice is possible. For (ii), the risk is a slight orientation mismatch between the bar and the insert, an alignment defect could lead to the generation of a moment at the interface. In both cases, although the specimen is still undergoing compression and tension, the input stress is not completely transmitted. The procedure used here to quantify the quality of these interfaces is the same as the one described in Saletti et al. (2019). The experimental ratio of the transmitted energy with the incident energy α_{exp} is compared with a theoretical value α_0 function of the bar and specimen impedances. The quality of the interfaces is assumed to be satisfying when the ratio α_{exp}/α_0 is close to 1. The ratios are presented in Table 2 for every succesful spalling test.

3 Results

3.1 2D characterization of the microstructure

The porosity being the parameter we focus on, we took care to provide specimens characterized by similar microstructures and crystallographic textures. Examples of thin sections analyzed with AITA are presented in Figure 5. We verified that the textures are isotropic and that grains are rather equiaxed. Grain areas have been measured by contour extraction and morphological tools from the orientation color-coded images obtained with AITA. The mean grain sizes in both microstructures range between 1 and 2 mm. This analysis shows that no significant difference is observed between the LP and HP microstructures and texture properties.

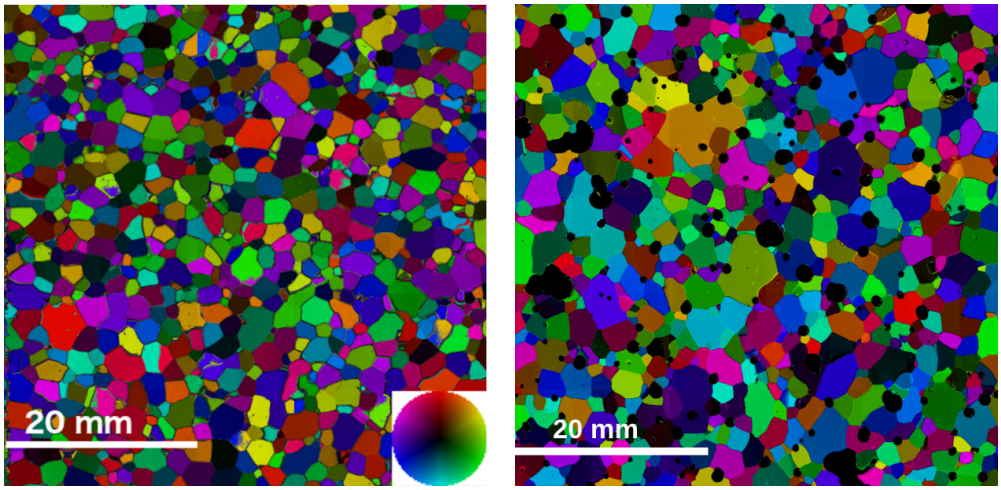

(a) (b)

Figure 5: (a) and (b) Microstructures represented colour-coded with the [0001] crystallographic axis (**c**-axis) orientation of LP and HP specimens respectively, as measured with the Automatic Ice Texture Analyzer from thin sections.

3.2 3D characterization of the microstructure with microCT

The low porosity specimens scanned for this study are LP10, LP11, and LP12, and the high porosity ones are HP12, HP13 and HP14. Figure 6 shows the distributions of porosity size and geometry for both microstructures as a function of a porosity equivalent radius. This equivalent radius is defined as the radius of a sphere whose volume is the one of the porosity. The coefficient of sphericity Ψ is computed as

$$\Psi = \frac{\pi^{1/3}(6V_p)^{2/3}}{A_p} \tag{2}$$

with V_p and A_p the volume and the surface of the ideal ellipsoid fitting the porosity. The technique described in Ikeda et al. (2000) was applied to recover the length of the principal axes. The main difference between the two microstructures is the presence of some large spherical porosities in the HP specimens, which equivalent radii exceed 0.3 mm. These large porosities are likely to exist prior to ice growth in the ice slurry mixture of HP specimens. Smaller porosities take random ellipsoid shapes and their formation is probably related to air trapped in the water. In the following, porosities will be splited into two populations : the population **A** (large spherical porosities) that only exist in HP specimens and the population **B** (small porosities with random ellipsoidal shapes), observed in both microstructures. Note that for a

scan at a given resolution, the uncertainty on porosity size and shape increases as the porosity size decreases. However scans performed at higher resolutions (not presented here) confirmed the random shape feature associated with population **B**.

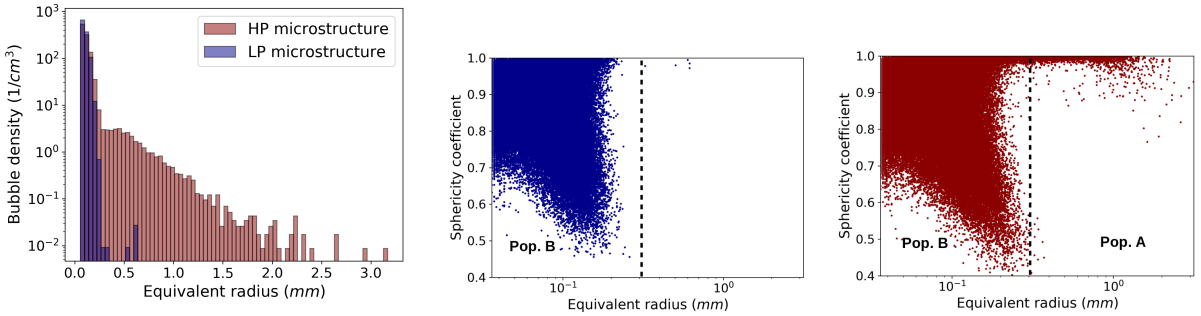

(a) (b) (c)

Figure 6: (a) porosity size distribution of LP11 (blue) and HP13 (red) specimens according to the porosity equivalent radius. Sphericity coefficient of each porosity for (b) LP and (c) HP specimens. The black dotted lines delimit the population **A** and **B**

3.3 Tensile strength measurements

The specimens LP12 and HP14 failed during the compression phase and were thus dismissed. The low quality of laser signals from LP10 and HP12 tests prevented the computation of their spalling strength. Consequently, we will treat only 12 spalling tests performed on HP specimens and 11 tests on LP specimens in the following. The relevant parameters directly measured or deduced from experimental signals, as detailed in section 2.4.2, are given in Table 2. The data obtained from LP specimens are extracted from Saletti et al. (2019) except LP09 and LP11 which are new tests. The strain rates range between 24 and 112 s^{-1} and between 41 and 120 s^{-1} for HP and LP specimens respectively. The measured spalling strengths, i.e. tensile strengths, vary between 0.8 to 3.0 MPa and from 1.9 to 5.3 MPa in the considered range of strain rate for HP and LP specimens, respectively.

The results presented in Figure 7 highlight an increase of the tensile strength with strain rate. A strength weakening with increasing porosity is also observable, LP ice appearing almost twice stronger than HP ice for the highest strain rates. Few tests on HP specimens exceed a strain rate of 80 s^{-1} as these specimens are more likely to fail in compression at high loading rates. Overall it is difficult for both microstructures to reach strain rates higher than 120 s^{-1}

Spec Id	V_p $(m.s^{-1})$	C_{ice} $(m.s^{-1})$	σ_{spall} (MPa)	$\dot{\varepsilon}$ (s^{-1})	α_{exp}/α_0
LP01	6.3	3040	4.34	107	1.04
LP02	3.3	2667	1.90	41	0.94
LP03	5.1	2917	4.02	121	1.05
LP04	5.3	2992	4.40	110	1.04
LP05	5.8	2963	4.08	108	1.07
LP06	5.7	2881	4.33	120	1.07
LP07	3.9	3010	3.79	83	1.08
LP08	3.8	2794	3.16	69	1.07
LP09	7.7	3216	5.30	87	1.03
LP11	3.2	2972	3.66	43	0.97
HP01	2.9	2743	1.33	36	0.99
HP02	4.1	2669	2.14	90	1.09
HP03	2.9	2371	1.48	31	1.03
HP04	2.9	2673	1.68	54	1.10
HP05	2.9	2645	1.43	53	1.02
HP06	3.9	2589	2.96	99	1.06
HP07	3.2	2636	2.02	53	1.14
HP08	2.4	2482	1.40	24	1.03
HP09	4.0	2674	1.80	112	1.07
HP10	2.5	2530	1.52	29	1.05
HP11	4.0	2753	2.13	60	0.99
HP13	2.6	2174	0.83	33	0.80

Table 2: Projectile velocity V_p, acoustic wave velocity into the specimen C_{ice}, spalling strength to failure σ_{spall} and calculated strain rate in the tensile phase $\dot{\varepsilon}$ for LP and HP specimens, as obtained from the treatment of laser and strain-gauges signals. α_{exp}/α_0 is the ratio between the experimental and theoretical transmitted energy

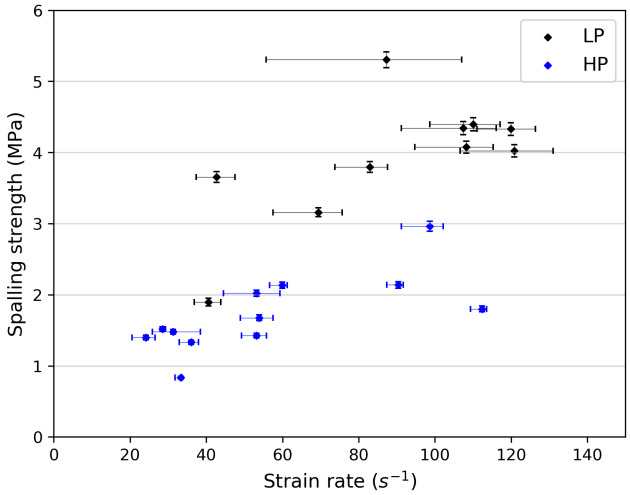

Figure 7: Tensile strength as a function of the strain rate. The displayed intervals on the curve correspond to the minimum and maximum values of strain rate measured during the tensile phase according to the elastic simulations. The marker (in between the intervals) corresponds to the mean values of the determined strain rates

with the experimental configuration used here.

3.4 Fragmentation analysis from UHS camera

The UHS camera allowed to observe the crack propagation in the volume of the specimen during each test. Although a qualitative piece of information, it enables to distinguish two main scenarios as a function of the strain rate. At low strain rates the ice experiences a single fragmentation occurring randomly in the volume loaded in tension as it can be observed in Figures 8a and 9a. At higher strain-rates the specimens undergo intense multiple fragmentations. In Figures 8b and 9b one can see several cracks oriented perpendicularly to the specimen axis expending in an initially restricted zone (white dashed-line rectangle). In the next steps of the test, this zone of damage spreads out toward the bar side of the specimens as observed on the last images. Finally, the higher the strain rate, the higher the crack density. However the quality of the images did not allow to find significant variations of the fragmentation pattern between LP and HP specimens.

3.5 Fragmentation analysis from AITA measurements

After spalling tests, post-mortem specimens were first scanned with the microCT (see section 3.6) and then brought back in cold rooms (-15°C) to perform thin sections and analyze the

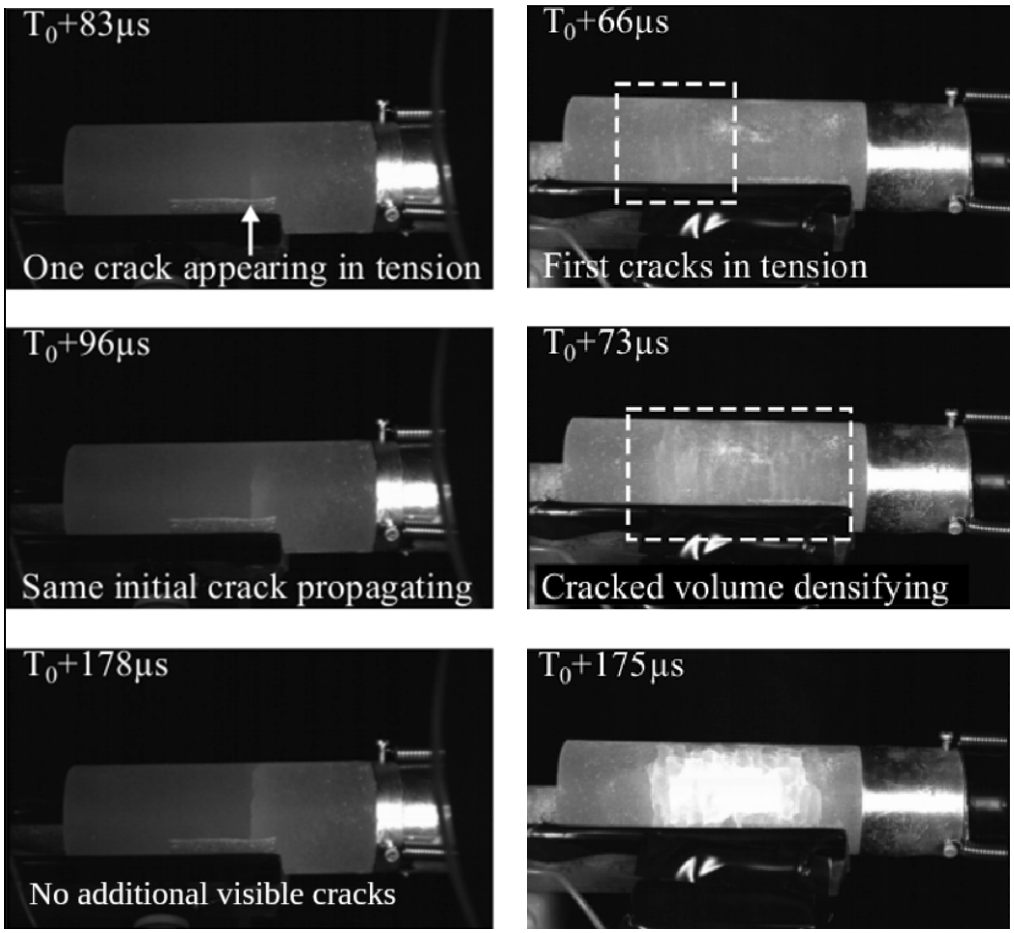

(a) # LP02 (41 s^{-1}) (b) # LP04 (110 s^{-1})

Figure 8: Fracture in LP specimens for two different strain rates.

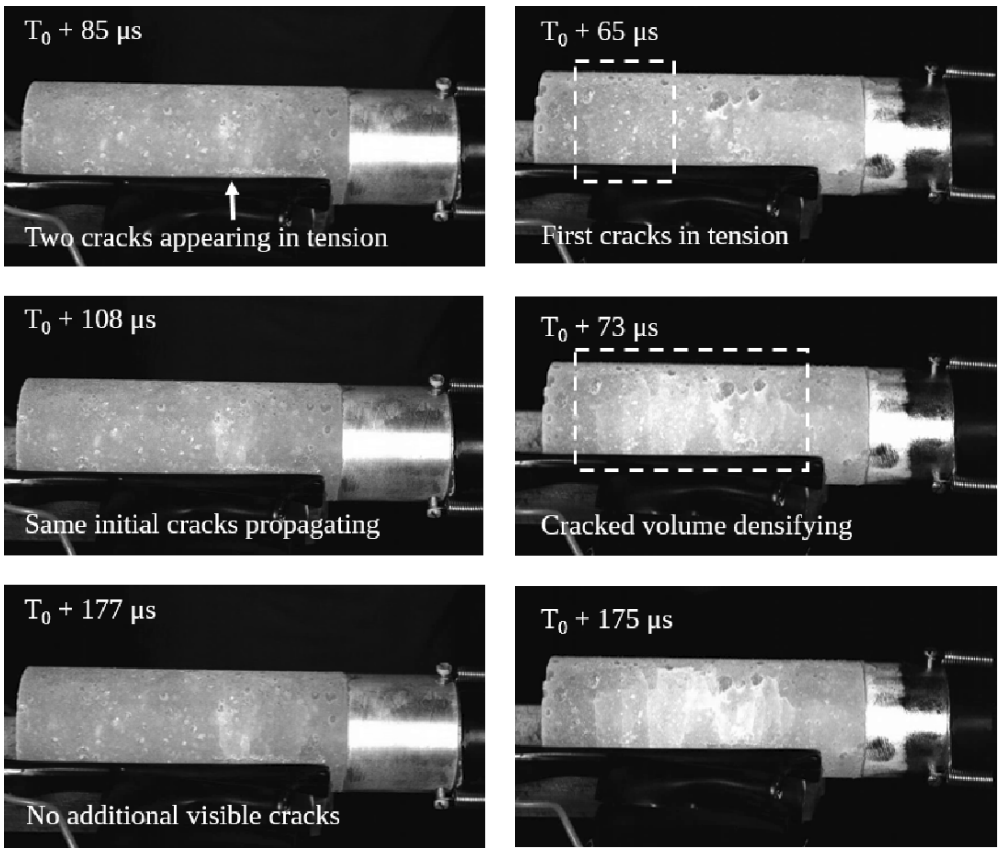

(a) # HP08 (24 s^{-1}) (b) # HP06 (99 s^{-1})

Figure 9: Fracture in HP specimens for two different strain rates.

cracked zones by using the Automatic Ice Texture Analyser. Areas of interest were selected around the fracture planes which could be located by eye. As described in section 2.2, 0.3 mm thick thin sections were made but a great care was taken not to create additional cracks during the operation. Pictures of the post-mortem specimens are shown in Figures 10 and 11, together with the corresponding thin sections analyzed with AITA. The cracks being very thin and therefore hardly visible on the pictures, there were manually highlighted by white lines added on the images. For specimens that fractured into two distinct fragments, a small gap was left between the two parts during the manufacturing of the thin sections (see Figures 10b and 11b).

Although one main plane of fracture is always observable, numerous additional cracks seem to have been triggered during the tests, which orientations are roughly perpendicular to the specimen principal axis. In each thin section a branching phenomenon or cracks coalescence can be seen, especially in the LP10 specimen. No clear evidence appears in our observations about a likely influence of the microstructure in the crack junction/separation as no cracks follow the grain boundaries and no distinct direction shift could be observed at a triple junction. However, in the analyzed HP microstructures, the cracks seem to follow a route through the largest porosities or to be trigerred from these porosities. The crack tip is generally located in a porosity, at least on the 2D images and for cracks not crossing the entire specimen. These observations have to be considered with caution considering the high density of large porosities in the volume and the fact that these images provide only 2D information. Regarding LP specimens, no evidence about some relationship between porosities and crack initiation and propagation could be established, due to a too low spatial resolution of the AITA analysis and the high density of small pores.

Unfortunately, the measurement chains were not successful for LP10 and HP12 : it was not possible to process these tests to get the spalling strength. Nevertheless, they both experienced tension during the test and UHS camera analysis reveals that no compression fractures occurred. Consequently their fragmentation pattern can still be presented in this paper as we consider they are representative of the micro-scale processes at play.

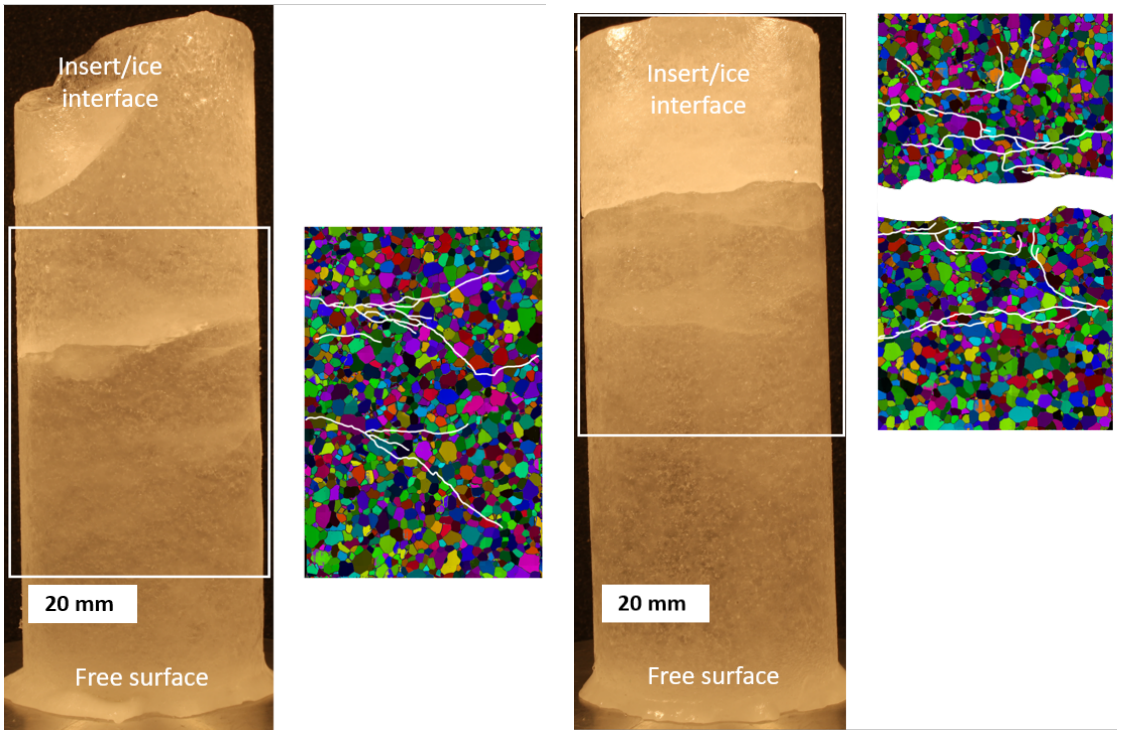

(a) LP10 (b) LP11

Figure 10: Post-spalling pictures and orientation color-coded microstructures of the cracked zones for two LP specimens. White lines on thin sections are manually added to make visible the crack network.

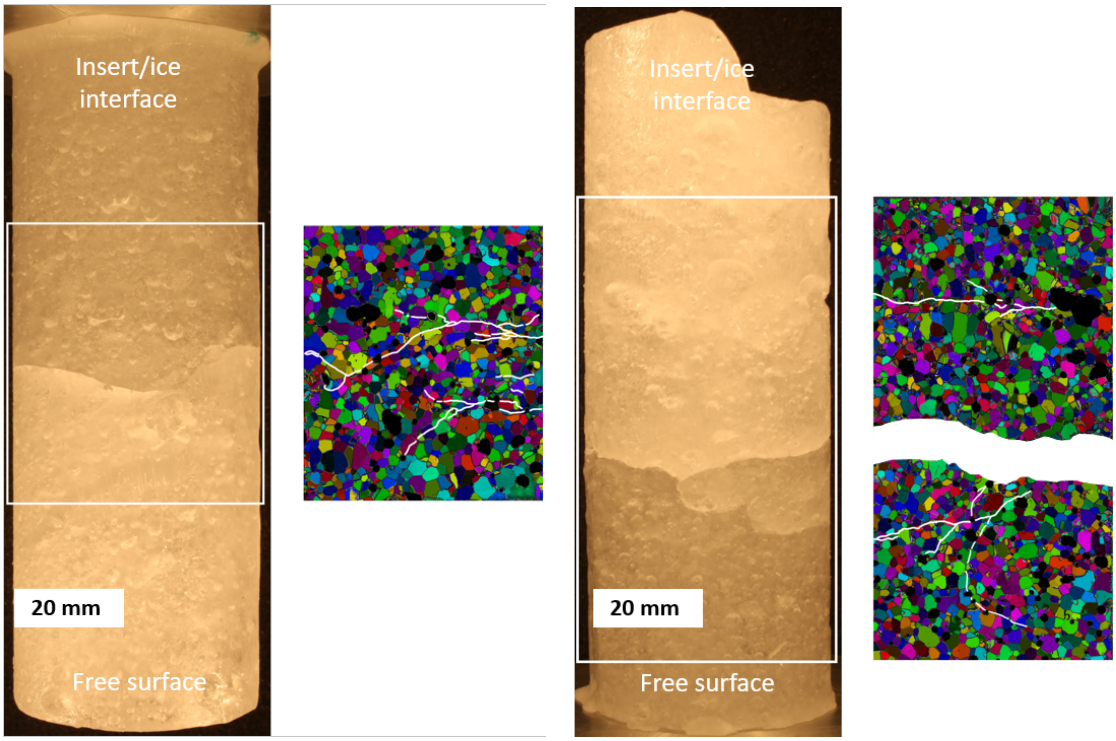

(a) HP12 (b) HP13

Figure 11: Post-spalling pictures and orientation color-coded microstructures of the cracked zones for two HP specimens. White lines on thin sections are manually added to make visible the crack network.

3.6 Fragmentation analysis from micro-CT measurements

LP10, LP11, HP12 and HP13 specimens were scanned within a few hours following the spalling tests, using the set-up and conditions described in section 2.3. The intense fragmentation during the spalling tests of LP12 and HP14 specimens prevented from carrying them to the micro-CT device. LP11 and HP13 specimens fractured into two pieces, fragments were put together back by taking care of a good match between them prior to scanning. We can expect some cracks healed between the spalling test and the micro-CT scans, as commonly observed when ice is subjected to a temperature gradient (Colbeck, 1986).

Examples of microCT images of cracked zones are presented in Figures 12 and 13. Except for fracture planes separating two fragments, the crack thickness appears not to exceed several microns. In addition, the grey values associated to crack volume lie in the ice value range, as shown on images (1) and (2) of Figure 12a, where impulse noise makes difficult or impossible to isolate the cracks. Consequently only the main fracture planes were efficiently identified. To do so, digital image correlation has been performed with SPAM on HP specimens by using the initial volumes scanned prior to spalling test and the fragmented volumes analyzed post-test. The transformation matrix from DIC treatment allowed to adjust the position of the two volumes. The only difference between the two scanned volumes being the fragmentation pattern, the largest cracks could be identified by substracting the two 3D images. The software SPAM gives access to the exact position of each voxel in the volume, porosities in contact with the different fracture planes could thus be collected. Results are shown on images (2) and (3) of Figures 13a and 13b. A simple thresholding method was applied for LP11 specimen to isolate the main fracture plane.

The crack observed in the LP11 specimen (Figure 12b) is almost perpendicular to the tensile loading direction, with no noticeable direction shift, and covers the entire specimen thickness. The same pattern is observable on 2D images obtained with micro-CT for the LP20 specimen. The situation is different for the fracture plane of specimen HP12 where the crack, although approximately perpendicular, is more tortuous and eventually stops before crossing the total thickness. Two cracks could be isolated in the HP13 specimen, one perpendicular to the speci-

406 men axis and another oriented at around $30 - 40°$ from this axis. The junction between these
407 cracks occurred nearby the specimen surface. From qualitative observations, the crack surfaces
408 seem to be slightly rougher in the HP microstructures than in the LP microstructures.

409

410 As for the 2D analyses performed in section 3.5, we can hardly conclude on a clear influence of
411 porosity on crack initiation and propagation. However porosities were detected on the surface
412 of each crack in every specimen analyzed from microCT 3D reconstructions.

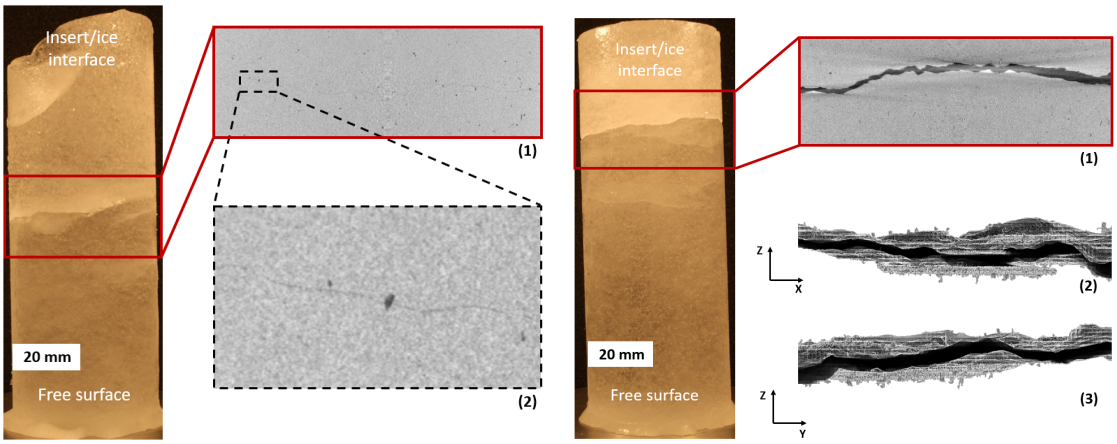

(a) LP10 (b) LP11

Figure 12: Observation of crack areas from microCT scans. a) specimen **LP10** : (1) 16 bits 2D image of the crack area, (2) Focus on the crack path. b) specimen **LP11** : (1) 16 bits 2D image of the crack area, (2) and (3) 3D crack visualisation according to XZ and YZ planes respectively.

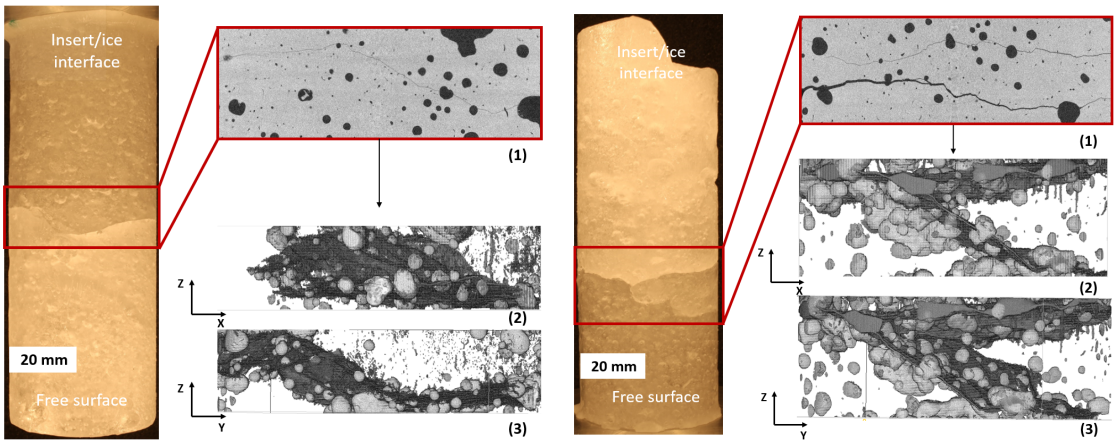

(a) HP12 (b) HP13

Figure 13: a) and (b): (1) 16 bits image of cracked zone, (2) and (3) 3D crack visualisation according to XZ and YZ planes respectively. The porosities in contact with crack networks are shown in white. Figures en cours de modification (suppression du bruit et amélioration du contraste pores/fissures)

4 Discussion

4.1 Strain-rate dependency of ice dynamic tensile strength

Results shown on Figure 7 evidence a strain-rate sensitivity of the dynamic tensile strength of ice, as already shown by Saletti et al. (2019) for the microstructure with a low porosity. This strain-rate hardening is a common feature found in many other brittle materials, such as concrete, ceramics, or rocks (Cho et al., 2003; Schuler et al., 2006; Zinszner et al., 2015; Saadati et al., 2016). Under quasi-static sollicitations, ice strength has been shown to be strain-rate insensitive and is rather subjected to microstructural property dependency (Schulson and Duval, 2009; Schulson, 2001). Based on results obtained from direct tensile tests and bending tests in the literature (Petrovic, 2003; Schulson and Duval, 2009; Timco and Weeks, 2010) , together with the results presented here, the transition between a strain-rate insensitive and a strain-rate sensitive response seems to occur approximately between 10^{-1} s^{-1} and 10^{1} s^{-1}. This transition phenomenon exists in many other brittle materials that show a probabilist behavior at low strain-rates and a deterministic behavior at higher rates of loading (Hild et al., 2003; Forquin and Hild, 2010). Despite the narrow strain-rate range covered here (24 s^{-1} to 120 s^{-1}), polycrystalline ice appears to follow the same trend, as the dispersion of tensile strength associated with spalling tests appears much lower than the one observed in the quasi-static regime (Timco et al., 1994).

To explain this macroscopic behavior, a point of view at a microscopic scale can be used. Indeed, microstructural defects (such as porosities, grain boundaries, micro-cracks, etc) are frequently considered as responsible for crack triggering in brittle materials under tension. The microscopic stress required to activate a critical defect is a complex function of the defect nature, size, orientation, etc... (Jayatilaka and Trustrum, 1977). Under quasi-static conditions, a single crack is likely to be responsible for the complete specimen failure. In the dynamic range, brittle materials undergo a multiple fragmentation, as observed on ice during spalling tests (Section 3.4) with a crack density increasing with strain rate. Denoual and Hild (2000) and Forquin and Hild (2010) introduced the concept of "critical defect obscuration" and "local weakest link hypothesis" to describe the fragmentation process in brittle solids and to predict the crack density and the tensile strength dependency with the applied strain rate. The theory lies on the growth

of obscuration zones which correspond to areas in which stress-release waves develops due to unstable cracks activated from the non-obscured critical defects. At low strain-rates, damage propagates to the full specimen prior to local stress increase, preventing any additional crack triggering. At high strain-rate, the limited crack speed makes possible a local stress increase, leading to the activation of a large number of cracks that propagate in small zones up to crack coalescence. Only when damaged volumes link up will the complete fragmentation of the material occur, which results into a higher macroscopic strength. As a consequence, crack density and strength is expected to increase with strain-rate.

The observations performed here on polycrystalline ice are in agreement with Forquin and Hild (2010) approach. Indeed, the high speed camera observations reveal an increase in the number of failure planes with strain rate (see Figures 8 and 9). Cracks are approximately perpendicular to the loading direction, meaning that they are mainly opening in mode I as a result of a brittle response to the tensile loading.

3D images of post-mortem specimens (Figures 12b, 13a and 13b) reveal rough and irregular profiles of crack at the microstructure scale, while the linear elastic fracture mechanics theory would predict straight cracks perpendicular to the maximum tensile stress, as long as the cracks do not interact with each other. On top of the impact of porosity on the crack propagation routes discussed in Section 4.2, the crack roughness could result from the coalescence of several small cracks. Although the limitations of our observation methods (AITA and microCT) and possible microcrack proofing, prevent from a quantitative evaluation of crack density, the observation of a relatively high number of small cracks in the vicinity of the main fracture plane would be consistent with the former hypothesis. Furthermore, would a single crack be responsible for the specimen failure, the failure process would take the minimum time for the crack to propagate through the specimen, that can be estimated at around 20 μs (equal to $r_{spec}/0.38C_{ice}$, $0.38C_{ice}$ being the supposed crack speed Ref) for specimen of radius 22.5 mm. In the case of specimen LP11, for instance, the time interval in the tensile phase to reach failure (roughly equal to $\sigma_{spall}/E\dot{\varepsilon}$) was about 9 μs, that is about twice shorter than the time for a crack to propagate from the specimen axis to its outer surface.

Based on these observations, we can hypothesise that the pullback velocity measured by the laser interferometer on the free surface of the specimen is indeed the result of the growth and interaction of several cracks, very likely triggered on critical defects that are supposed to be the porosities, and that the coalescence results into a macroscopic fracture plane.

4.2 Porosity effects on ice dynamic tensile strength

The strain-rate effect discussed above, although noticeable for both microstructures, is less pronounced for the HP microstructure. Both LP and HP microstructures have been designed to be similar in terms of grain size and shape, and crystallographic orientation, but to present two different porosities. The main difference between the two microstructures come from the presence, in the HP specimens, of large spherical porosities (population **A**). We therefore make the hypothesis that the difference observed in dynamic tensile strength between the two types of specimens arises, in a direct or indirect way, from the role of porosities. Porosities are microstructure defects and therefore potential areas of stress concentration during tensile loading. Two processes could be involved, namely initiation of new cracks or/and the influence of porosities on crack propagation.

Crack initiation

Several studies point out a link between the size of a microstructural defect and a corresponding critical stress for crack nucleation. Liu (1997) showed that increasing the pore size for a given porosity induced a decrease in the compressive strength of porous ceramics. Chao et al. 1992 evidenced that the fracture strength distribution in sintered silicon nitride under tensile loading could be predicted from the pore size distributions. Recently, Forquin et al. (2019a) hypothesized that the porosities population found in an ultra-high performance concrete, a ceramic and porous ice could be considered to model single and multiple fragmentation properties of these materials.

Under dynamic loadings, as described in the DFH obscuration model (Denoual and Hild, 2000; Forquin and Hild, 2010), the differences observed in the dynamic responses of two materials

having distincts microstructural properties would arise from the activation of different defect populations. In this study, if we assume that the porosities are the only critical defects of the microstructures considered and that the threshold stress for crack triggering is depending on the pore size, the porosity weakening effect could be due to a premature fragmentation in HP specimens. The porosities belonging to population **A** (present only in HP specimens) would initiate cracking phenomenoms at lower stresses than porosities from population **B** (present in both types of microstructures). At very high strain-rates (not reached here) and if the aforementioned hypothesis are still valid, one could expect similar dynamic behavior from LP and HP specimens as the pore size distributions for small porosities tend to be the same in both microstructures.

Although the 2D or 3D analyses of post-mortem specimens presented here are not accurate enough to clearly identify the role of porosities in crack triggering, we observed a large number of porosities from population **A** located along cracks in HP specimens. In addition, porosities from population **B** adjacent to cracks in LP specimens were also detected on the microCT images (see for instance the image 2 of Figure 12a) . On top of that, cracks propagate through the grains (see Figures 5a and 5b) implying that grain boundaries or at a triple junction are not major initiation areas.

Crack propagation

As shown previously (Section 3.4), and as usually observed for quasi-brittle materials, the crack density is increasing with strain-rates. The main explanation comes from the limited crack velocity that restricts the growth of obscuration volumes making possible the activation of more cracks on non-obscured critical defects. However, under quasi-static loadings or at moderate strain-rates when the material is not highly fragmented (as the ones undergone by LP10, LP11, HP12 and HP13 for instance), crack propagation could be dependent on the presence of microstructural defects. Renard et al. (2009) showed that mechanical heterogenities (such as pores and grains) in rocks may affect a fracture propagation by acting on the stress field near a crack tip under quasi-static loading. They observed an attraction phenomenom from porosities on

the final crack path hence a subsequent amplitude of its out-of-plane fluctuations. Chen et al. (2016) investigated the effect of pores on the stress-intensity factors of the crack tips in porous ceramics, by using the J-integral numerical method. Pores in front of the propagating cracks was found to promote crack propagation by enhancing the stress intensity factor of the crack tip. For ice material, Smith et al. (1990) experimentally established a porosity weakening of ice fracture toughness, implying porosity would facilitate crack propagation. Here, rough and wavy crack paths described in section 3.6 tell us about a likely role of porosity on crack propagation prior to failure. The presence of large spherical porosities on the crack path (Figures 11 and 13) could illustrate how porosities would distord the crack propagation resulting in the roughness and out-of-plane fluctuations observed on crack surfaces of HP specimens. Also, the redistribution of the stress-field ahead of a crack tip could potentially activate new micro-cracks on porosities into the vicinity of the crack (Ref). Based on the work of Smith et al. (1990) and regarding the high density of porosities from population **A**, we can expect significantly lower fracture toughness in HP specimens compared to LP ones. Thus, micro-cracks coalescence is probably more efficient in the highly porous specimens, hence a faster damage propagation in the latters inducing lower tensile strength to failure.

5 Conclusion

Following on the work of Saletti et al. (2019), we performed spalling tests on polycrystalline ice. Specimens with two different levels of porosity were considered in order to study the porosity effect on the dynamic response of ice under tensile loading. Fragmentation processes were also investigated on post-mortem specimens by means of an Automatic Ice Texture Analyser (AITA) and a micro-Tomograph (TOMOCOLD). A strain-rate hardening of the tensile strength and the crack density have been observed for both microstructures over the range 24 s^{-1} to 120 s^{-1}, as expected for a material exhibiting a brittle behavior. However, porosity seems to weaken the ice tensile strength, the strain-rate influence being less marked with highly porous ice. The presence of large spherical porosities in highly porous specimens is thought to be responsible of the porosity weakening observed, as no additional differences could be detected between the two microstructures. The role of these porosities has been discussed in term of crack initiation

and propagation. We made the assumption that the critical stress susceptible to initiate a crack from a porosity is function of the porosity size, leading to a premature activation of the large spherical porosities in highly porous ice. This theory is supported by the high density of porosities located along crack paths. Rough crack surfaces observed in 2D and 3D analysis also show that porosities potentially accelerated the crack propagation and crack coalescence. All these observations tend to confirm the role of porosity as a key parameter to describe the dynamic behavior of ice subjected to tensile loading.

Aknowledgements

The present work was developed in the framework of the Brittle's Codex chair (Fondation UGA) and thanks to the support from the CEA-CESTA and from the Labex OSUG@2020 (ANR 10 LABEX 56). The provided support and fundings are gratefully acknowledged by the authors.

References

Barnes, P., Tabor, D., and Walker, J. (1971). The friction and creep of polycrystalline ice. *Proc. R. Soc. Lond. A*, 324(1557):127–155.

Carney, K. S., Benson, D. J., DuBois, P., and Lee, R. (2006). A phenomenological high strain rate model with failure for ice. *International Journal of Solids and Structures*, 43(25-26):7820–7839.

Chen, M., Wang, H., Jin, H., Pan, X., and Jin, Z. (2016). Effect of pores on crack propagation behavior for porous si3n4 ceramics. *Ceramics International*, 42(5):5642–5649.

Cho, S. H., Ogata, Y., and Kaneko, K. (2003). Strain-rate dependency of the dynamic tensile strength of rock. *International Journal of Rock Mechanics and Mining Sciences*, 40(5):763–777.

Colbeck, S. (1986). Theory of microfracture healing in ice. *Acta metallurgica*, 34(1):89–95.

Denoual, C. and Hild, F. (2000). A damage model for the dynamic fragmentation of brittle solids. *Computer methods in applied mechanics and engineering*, 183(3-4):247–258.

Dousset, S. (2019). Comportement mécanique dynamique de la glace: Contributions expérimentales et numériques pour le cas d'impacts de grêle sur structure aéronautique.

Erzar, B. and Forquin, P. (2010). An experimental method to determine the tensile strength of concrete at high rates of strain. *Experimental Mechanics*, 50(7):941–955.

Erzar, B. and Forquin, P. (2011). Experiments and mesoscopic modelling of dynamic testing of concrete. *Mechanics of Materials*, 43(9):505–527.

Erzar, B. and Forquin, P. (2014). Analysis and modelling of the cohesion strength of concrete at high strain-rates. *International Journal of Solids and Structures*, 51(14):2559–2574.

Forquin, P. (2017). Brittle materials at high-loading rates: an open area of research.

Forquin, P., Blasone, M., Georges, D., Dargaud, M., and Ando, E. (2019a). Modelling of the fragmentation process in brittle solids based on x-ray micro-tomography analysis. *24ème Congrès Français de Mécanique, Brest, 26 au 30 Août 2019*, 2019.

598 Forquin, P. and Hild, F. (2010). A probabilistic damage model of the dynamic fragmentation
599 process in brittle materials. In *Advances in applied mechanics*, volume 44, pages 1–72.
600 Elsevier.

601 Forquin, P., Lukić, B., Saletti, D., Sallier, L., and Pierron, F. (2019b). A benchmark testing
602 technique to characterize the stress–strain relationship in materials based on the spalling
603 test and a photomechanical method. *Measurement Science and Technology*, 30(12):125006.

604 Forquin, P., Sallier, L., and Pontiroli, C. (2015). A numerical study on the influence of free water
605 content on the ballistic performances of plain concrete targets. *Mechanics of Materials*,
606 89:176–189.

607 Hild, F., Denoual, C., Forquin, P., and Brajer, X. (2003). On the probabilistic–deterministic
608 transition involved in a fragmentation process of brittle materials. *Computers & Structures*,
609 81(12):1241–1253.

610 Ikeda, S., Nakano, T., and Nakashima, Y. (2000). Three-dimensional study on the interconnec-
611 tion and shape of crystals in a graphic granite by x-ray ct and image analysis.

612 Jayatilaka, A. d. S. and Trustrum, K. (1977). Statistical approach to brittle fracture. *Journal*
613 *of Materials Science*, 12(7):1426–1430.

614 Kermani, M., Farzaneh, M., and Gagnon, R. (2008). Bending strength and effective modulus of
615 atmospheric ice. *Cold regions science and technology*, 53(2):162–169.

616 Keune, J. (2004). *Development of a hail ice impact model and the dynamic compressive strength*
617 *properties of ice*. PhD thesis, MS thesis, Purdue University West Lafayette.

618 Kim, H. and Kedward, K. T. (2000). Modeling hail ice impacts and predicting impact damage
619 initiation in composite structures. *AIAA journal*, 38(7):1278–1288.

620 Kim, H. and Keune, J. N. (2007). Compressive strength of ice at impact strain rates. *Journal*
621 *of materials science*, 42(8):2802.

622 Klepaczko, J. and Brara, A. (2001). An experimental method for dynamic tensile testing of
623 concrete by spalling. *International journal of impact engineering*, 25(4):387–409.

624 Lange, M. A. and Ahrens, T. J. (1983). The dynamic tensile strength of ice and ice-silicate
625 mixtures. *Journal of Geophysical Research: Solid Earth*, 88(B2):1197–1208.

626 Liu, D.-M. (1997). Influence of porosity and pore size on the compressive strength of porous
627 hydroxyapatite ceramic. *Ceramics International*, 23(2):135–139.

628 Lukić, B. B., Saletti, D., and Forquin, P. (2018). On the processing of spalling experiments.
629 part ii: identification of concrete fracture energy in dynamic tension. *Journal of Dynamic*
630 *Behavior of Materials*, 4(1):56–73.

631 Macklin, W. C., Knight, C. A., Moore, H. E., Knight, N. C., Pollock, W. H., Carras, J. N., and
632 Thwaiters, S. (1977). Isotopic, crystal and air bubble structures of hailstones. *Journal of*
633 *the Atmospheric Sciences*, 34(6):961–967.

634 Mazars, J. (1984). Application de la mécanique de l'endommagement au comportement non
635 linéaire et à la rupture du béton de structure. *THESE DE DOCTEUR ES SCIENCES*
636 *PRESENTEE A L'UNIVERSITE PIERRE ET MARIE CURIE-PARIS 6*.

637 Novikov, S., I.I., D., and A.G., I. (1966). The study of fracture of steel, aluminium and copper
638 under explosive loading. *Fizika Metallov i Metallovedenie*, 21:608.

639 Ortiz, R., Deletombe, E., and Chuzel-Marmot, Y. (2015). Assessment of damage model and
640 strain rate effects on the fragile stress/strain response of ice material. *International Journal*
641 *of Impact Engineering*, 76:126–138.

642 Park, H. and Kim, H. (2010). Damage resistance of single lap adhesive composite joints by
643 transverse ice impact. *International Journal of Impact Engineering*, 37(2):177–184.

644 Pernas-Sánchez, J., Pedroche, D., Varas, D., López-Puente, J., and Zaera, R. (2012). Numerical
645 modeling of ice behavior under high velocity impacts. *International Journal of Solids and*
646 *Structures*, 49(14):1919–1927.

647 Petrovic, J. (2003). Review mechanical properties of ice and snow. *Journal of materials science*,
648 38(1):1–6.

649 Pierron, F. and Forquin, P. (2012). Ultra-high-speed full-field deformation measurements on

concrete spalling specimens and stiffness identification with the virtual fields method. *Strain*, 48(5):388–405.

Renard, F., Bernard, D., Desrues, J., and Ougier-Simonin, A. (2009). 3d imaging of fracture propagation using synchrotron x-ray microtomography. *Earth and Planetary Science Letters*, 286(1-2):285–291.

Saadati, M., Forquin, P., Weddfelt, K., and Larsson, P.-L. (2016). On the tensile strength of granite at high strain rates considering the influence from preexisting cracks. *Advances in Materials Science and Engineering*, 2016.

Saletti, D., Georges, D., Gouy, V., Montagnat, M., and Forquin, P. (2019). A study of the mechanical response of polycrystalline ice subjected to dynamic tension loading using the spalling test technique. *International Journal of Impact Engineering*, page 103315.

Schuler, H., Mayrhofer, C., and Thoma, K. (2006). Spall experiments for the measurement of the tensile strength and fracture energy of concrete at high strain rates. *International Journal of Impact Engineering*, 32(10):1635–1650.

Schulson, E. M. (2001). Brittle failure of ice. *Engineering fracture mechanics*, 68(17-18):1839–1887.

Schulson, E. M. and Duval, P. (2009). *Creep and fracture of ice*. Cambridge University Press.

Shazly, M., Prakash, V., and Lerch, B. A. (2009). High strain-rate behavior of ice under uniaxial compression. *International Journal of Solids and Structures*, 46(6):1499–1515.

Smith, T., Schulson, M., and Schulson, E. (1990). The fracture toughness of porous ice with and without particles. In *Proceedings, Ninth International Conference on Offshore Mechanics and Arctic Engineering*, pages 241–246.

Timco, G. et al. (1994). Flexural strength equation for sea ice. *Cold Regions Science and Technology*, 22(3):285–298.

Timco, G. and Weeks, W. (2010). A review of the engineering properties of sea ice. *Cold regions science and technology*, 60(2):107–129.

Tippmann, J. D., Kim, H., and Rhymer, J. D. (2013). Experimentally validated strain rate dependent material model for spherical ice impact simulation. *International Journal of Impact Engineering*, 57:43–54.

Wilson, C. J., Russell-Head, D. S., and Sim, H. M. (2003). The application of an automated fabric analyzer system to the textural evolution of folded ice layers in shear zones. *Annals of Glaciology*, 37:7–17.

Wu, X. and Prakash, V. (2015). Dynamic strength of distill water and lake water ice at high strain rates. *International Journal of Impact Engineering*, 76:155–165.

Zinszner, J., Forquin, P., and Rossiquet, G. (2015). Experimental and numerical analysis of the dynamic fragmentation in a sic ceramic under impact. *International Journal of Impact Engineering*, 76:9–19.